Reduced Graphene Oxide-based Flexible Pressure Sensor for Biomedical Applications

Reduced Graphene Oxide-based Flexible Pressure Sensor for Biomedical Applications

Alessandro Sanginario, *Member, IEEE*, Irene Buraioli, *Member, IEEE*, Marco Boscherini, *Member, IEEE*, Stefania Vitale, Conoci Sabrina, Daniele Botto, Dario Leone, Alberto Milan, Artur Ciesielski, Paolo Samorì and Danilo Demarchi, *Senior Member, IEEE*

***Abstract*— Pressure sensing is a crucial technique for various biomedical applications, where it can provide valuable information about the health and function of different organs and systems. This paper reports the development of a novel integrated pressure sensor based on modified rGO, a graphene-derivative material with enhanced piezoresistive properties. The sensor is fabricated on a flexible PCB substrate and conditioned by a smart current-based Wheatstone bridge circuit, which enables high sensitivity, wide detection range, fast response and recovery, and good stability under cyclic loading. The sensor achieves a measured sensitivity of 0.281 kPa^{-1} (at 0.5 kPa load). A mechanical system is also designed to adapt the sensor to different anatomical sites and to improve its elastic recovery. The sensor's functionality is initially demonstrated through its response to controlled mechanical stimulation, achieving a signal-to-noise ratio (SNR) of 25 dB. Subsequently, in a practical application, physiological signals from the carotid and femoral arteries of volunteers were acquired. The system effectively captured the pulse waveforms with high fidelity and accuracy (23.5 dB SNR) and measured the pulse transit time, an important parameter for estimating the pulse wave velocity and arterial stiffness. The sensor is not limited to this specific application and can be easily extended to other domains where pressure sensing is required. In conclusion, it offers a low-cost, flexible, and user-friendly solution for non-invasive biomedical monitoring and diagnosis.**

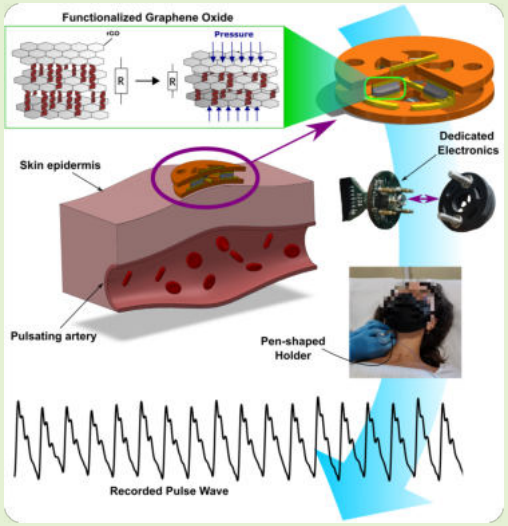

***Index Terms*— Biomedical Pressure Sensor, Current-based Wheatstone Bridge, Flexible PCB Sensor, rGO-based Pressure Sensor.**

I. Introduction

PRESSURE sensors are key tools for improving the quality of our planet as they offer vital functionalities enabling major steps forward in numerous upcoming technologies including robotics, biomedical devices for health monitoring and digital health care [1], environmental monitoring [2], wearables and foldable devices for human-machine interfaces and electronic skin (E-skin) [3]. In the field of biomedical technologies, they hold great significance as non-invasive tools for monitoring several vital signs, contributing to an effective improvement of medical diagnosis. Within the cardiovascular field, they employed not only for the heartbeat surveillance but also for the analysis of the arterial pulse wave to calculate the pulse wave velocity (PWV), considered a key parameter to assess arterial stiffness [4]–[6]. These sensors are also adept at monitoring breath rates through wearable devices, enabling a smart detection of respiratory dynamics [7], [8]. Additionally, pressure and strain sensing systems have been widely considered for human motion and step monitoring for rehabilitation purposes [9]–[11].

Ideally, an effective and reliable pressure sensor should meet several key requirements: high sensitivity is necessary to spot subtle pressure variations [12]–[14]; a wide detection range ensures versatility across multiple applications [15]; fast time response and recovery enables a correct acquisition of high-frequency pressure pulses and vibrations [16]–[18]; flexibility enhances the mechanical and electrical properties of the de-

Alessandro Sanginario, Irene Buraioli, Marco Boscherini, and Danilo Demarchi are with the Department of Electronics and Telecommunications, Politecnico di Torino, 10129 Torino, Italy (e-mail: alessandro.sanginario@polito.it; irene.buraioli@polito.it; marco.boscherini@polito.it; danilo.demarchi@polito.it).

Dario Leone and Alberto Milan are with the Candiolo Cancer Institute FPO-IRCCS, Division of Internal Medicine, Department of Medical Science - University of Turin, 10060 Candiolo (TO), Italy (e-mail: dario.leone@ircc.it; alberto.milan@ircc.it).

Daniele Botto is with the Department of Mechanical and Aerospace Engineering, Politecnico di Torino, 10129 Torino, Italy (e-mail: daniele.botto@polito.it).

Sabrina Conoci is with the Department of Chemical, Biological, Pharmaceutical and Environmental Sciences, University of Messina, 98122 Messina, Italy (e-mail: sabrina.conoci@unime.it)

Stefania Vitale, Artur Ciesielski and Paolo Samorì are with CNRS ISIS Université de Strasbourg, Strasbourg 67000, France (e-mail: svitale@unistra.fr; ciesielski@unistra.fr, samori@unistra.fr).

vice, improves the sensitivity and is fundamental for wearable applications [19]; stability and robustness are important parameters as they determine the sensor's repeatability over time and lifespan [9], [20]. However, the development of sensors that combine all these advanced characteristics represents a major challenge in the field of device engineering. Depending on the application target, a trade-off between these characteristics must be carefully considered to optimize the sensor's performance. With this purpose, various design strategies have been explored. Most of them encompass advanced material selection, surface functionalization, micro-structure use, and optimization of geometric shapes and device architectures. Chen et al. [21] achieved a satisfying compromise among the main features previously listed. They developed a pressure sensor based on hierarchical conductive fabric, resulting in high sensitivity (15.78 kPa^{-1}), a wide-detection range (30 Pa to 700 kPa), and excellent stability against deformation. Bai et al. [22] fabricated an iontronic flexible pressure sensor that demonstrated high sensitivity (49.1 kPa^{-1}) and linearity ($R2 > 0.995$) across a broad working range (up to 485 kPa). Moreover, such devices featured a fast response (< 5 ms), enabling the detection of high-frequency pressure changes.

The fabrication of pressure sensors is strictly related to the transduction mechanism used to convert pressure into an electrical output, which depends on the material and the structure of the device [23]–[25]. Resistive pressure sensors utilize the piezoresistive effect, wherein the deformation of the sensing element (often a flexible diaphragm) leads to a resistivity variation, detectable with proper conditioning circuits. These types of sensors have been widely used for fundamental research and industrial applications due to their good characteristics in terms of sensitivity, sensing range, simplicity of manufacturing process, and signal acquisition. [26] Many different types of conductive carbon-based materials with an extended variety of designs have been employed to fabricate piezoresistive sensors [12], [27]–[33]. In piezocapacitive devices, the input pressure leads to a capacitance variation due to a change in the dielectric layer's dielectric constant in the distance between plates or their area [23], [34]. Capacitive sensors offer several advantages, such as stability, broad working range, and the possibility of proximity sensing [35]–[37]. However, these sensors' limitations lie in a slower response and recovery time concerning other technologies. Piezoelectric materials have also been employed to perform pressure measurements, thanks to their capacity to generate charges in response to the application of an external pressure [23], [38]. Their main characteristics are the capability to produce instantaneous voltage pulses, resulting in a very high-speed response, excellent sensitivity, and robustness. For this reason, they have been extensively utilized for collecting high-frequency pressure stimuli [39], [40]. However, they are unsuitable for static pressure acquisitions due to the pulsed nature of the output electrical signals.

Over the last couple of decades, graphene has stood out as a highly interesting material for designing piezoresistive pressure sensors, as it exhibits unique properties [41]–[46]. In fact, its highest conductivity ($10e^6$ S/m at room temperature), resulting from a high electron mobility and saturation velocity, makes graphene suitable for electronic devices [47], [48]. On the other hand, its great elastic modulus E (> 1 TPa) and stretchability ($> 20\,\%$) confer to this material exceptional mechanical characteristics [49]. It's well-known that the sensitivity of a piezoresistive film is directly proportional to its thickness: for this reason, graphene, with its theoretical thickness of a single atom, is one of the most promising platforms for pressure sensors [50]. However, most research predominantly focuses on graphene derivatives, such as reduced graphene oxide (rGO). rGO, while exhibiting limited potential compared to pristine graphene in terms of electrical and mechanical properties due to its lower electrical conductivity and the presence of structural defects, offers greater scalability and ease of processability, making rGO-based pressure sensors more applicable for a wide range of uses [42], [51]–[55]. In a study by Tian et al. [56], a resistive pressure sensor consisting of laser-scribed graphene (LSG) films, derived from the reduction of graphene oxide, was presented. The characterization of the LSG sensor demonstrated notable results in terms of sensitivity (up to 0.96 kPa^{-1}) across a moderate operational range (0 to 50 kPa).

In this work, we have exploited an already established sensory material based on chemically functionalized GO [57] and integrated this into a novel pressure sensor architecture. The novelty resides in the synergy between the integrated rGO-based transducing material, the shape of the sensor, and the widely available substrate technology.

The manuscript's organization is the following: section II explores sensor design and fabrication characteristics, detailing considerations and characterizations crucial for developing the system's sensors. Moving on to Section III, the reading system is examined, focusing on the mechanisms and technologies responsible for interpreting signals from the sensors and converting raw data into meaningful information. Section IV focuses on firmware, delving into its crucial functions, algorithms, and role in ensuring proper operation and communication between system components. Section V introduces the graphical user interface, discussing the design and functionality of the interface that users interact with, encompassing aspects such as user experience and visual design. Section VI then explores the practical applications of the system, detailing its intended use cases and how it addresses a specific case scenario. Finally, in Section VII, the conclusions provide a comprehensive summary of key findings, contributions, and implications, touching on challenges, potential future research directions, and the overall significance of the project in a broader context.

II. Sensor Design and Fabrication

The preparation of sensing material has been described in [57]. To help the reader, in subsection II-A, we briefly recall its fabrication process. The subsequent sections present sensor assembly and characterization from both technological and mechanical standpoints.

A. rGO-R1 Fabrication process

The pressure sensing devices were prepared using a graphene-based material, rGO-R1, as a piezoresistive active

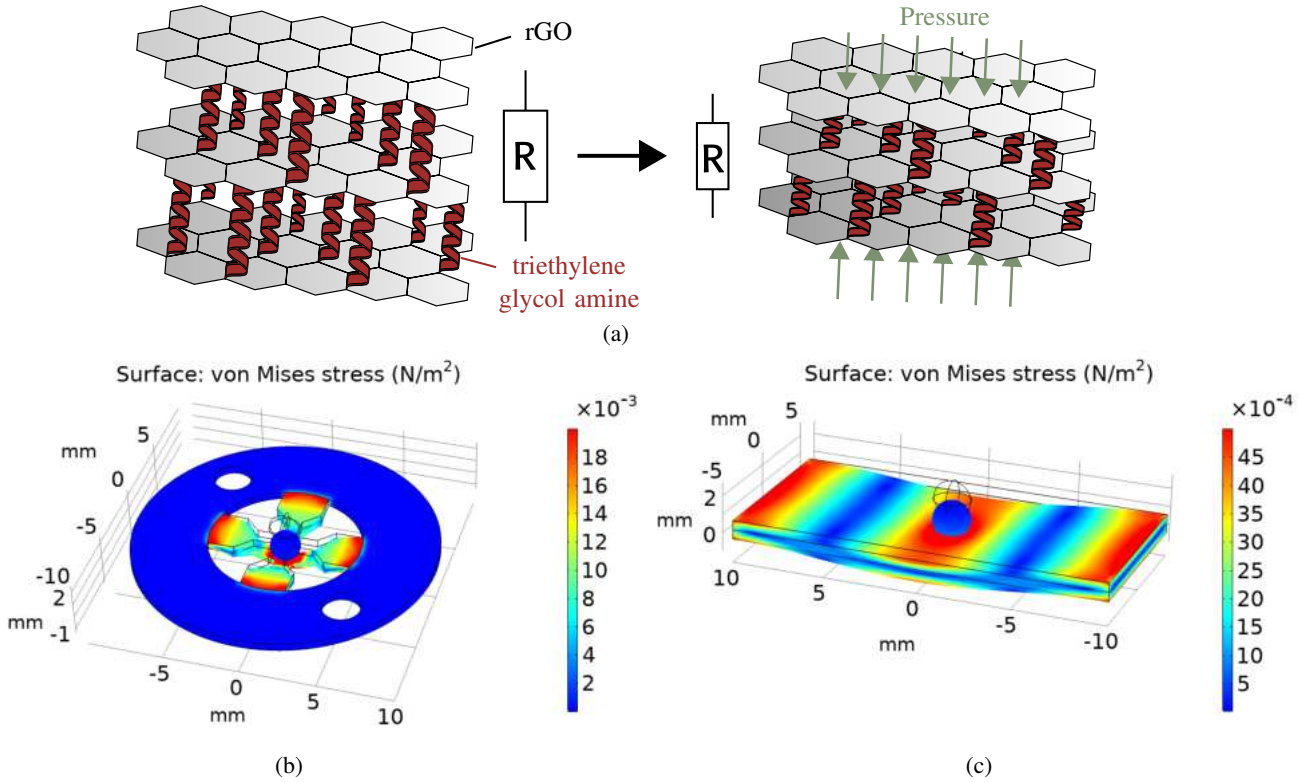

Fig. 1: (a) The triethylene glycol amine (R1) acts as a microscopic spring thanks to its mechanical flexibility. When compressed, the interlayer distance between the rGO sheets decreases, consequently reducing resistivity. Therefore, using a spring with a contour length less than 2 nm imposes a spacing between lower than such a size; electronic cross-talk between adjacent graphene flakes in the stacks will be ruled by tunneling. This is key as its exponential relation between the measured current and the inter-flake distance endows a high sensitivity to tiny distance changes. [57] (b,c) COMSOL Multiphysics® simulations to detect the maximum stress areas in the case of (b) cross-shaped and (c) rectangular sensor geometries.

component [57]. Such active material consists in reduced graphene oxide functionalized with the flexible molecular linker triethylene glycol amine. This was already shown to display excellent piezoresistive behavior compared to simple rGO, with a greatly enhanced response to the applied pressure in the 0.05-0.1 kPa range. rGO-R1 was used to assemble a flexible pressure sensing device, which exhibited excellent properties in terms of sensitivity (as high as 0.82 kPa^{-1}), response time (24 ms), detection limit (7 Pa), durability (over 2000 cycles), and flexibility. Firstly, graphene-based active material, rGO-R1, was prepared following a previously reported synthetic procedure consisting of two main steps: i) the reaction of graphene oxide (GO) with triethylene glycol amine, followed by ii) chemical reduction with $N_2H_4 \cdot H_2O$. Both reactions i) and ii) were carried out by stirring overnight under reflux at 90°C, under N_2 atmosphere, followed by purification through a sonication-centrifugation process (three cycles of 10 min at 2000 rpm). The resulting product, rGO-R1, was suspended in ethanol for a working dispersion of 0.5 mg/mL.

B. Working principle

The proposed sensor comprises a thin layer of rGO-R1 deposited on a conductive surface. Utilizing a diaphragm as a flexible membrane, the sensor reacts to applied pressure by bending, consequently altering the resistance of the rGO-R1 layer (Fig. 1a). This change in resistance correlates directly with the amount of strain and is typically measured via a Wheatstone bridge. Like all piezoresistive sensors, the primary objective is to augment sensitivity by increasing the strain applied to the sensor. For this reason, considering the test case on which we validated the sensor, dedicated simulations were performed to assess the best position to deposit the piezoresistive material corresponding to the maximum stressed areas. Without going into details of the substrate, which will be described in section II-D, we performed finite element (FE) simulations to locate the point of maximum deflection in the case of two different geometries: a rectangular one to directly compare with the substrate used in the previous work and a cross-shape one to increase the sensitivity.

C. Simulations

The circular crown of the sensor was imposed to be mechanically fixed (blu colored in Fig. 1b), and a rounded-tip cylinder (represented only as a sphere in the simulation) with a diameter of 2 mm was placed at the center of the cross. Finally, a load of 0.5 N was applied to the cylinder. Similarly, the rectangular sensor was mechanically fixed on its extremities (Fig. 1c) with the same rounded cylinder tip simulating the load. Results, respectively shown in Fig.1b and Fig.1c, indicate the maximum deflection to be located on the edge between

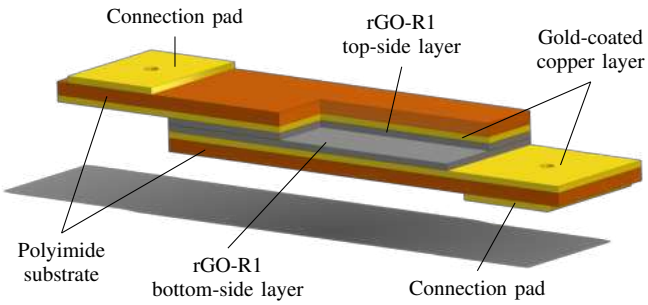

Fig. 2: Partial cross-section of the rectangular-shaped sensor. The polyimide tape surrounding the sensor is not depicted. Image not to scale.

the arms of the cross and the fixed circular crown and the center of the cross. In the case of the rectangular sensor, its stress distribution profile resembles that of the first shape, with notable stress concentrations at the edges and center. As expected, stress values of cross-shaped geometry are more than one order of magnitude higher. These results indicate that the cross-shaped sensor could obtain a better sensitivity with a more compact design; therefore, it could be the shape in which to invest our development efforts.

D. Sensor fabrication process

The substrate used in [57] was a rectangular cut out of indium tin oxide (ITO) coated poly(ethylene terephthalate) (PET). To overcome problems emerging with the asymmetric nature of the electrical contacts and the manual cutting procedure that could only output simple geometries, a very common yet technologically advanced substrate was chosen: polyimide Printed Circuit Boards (PCB). Polyimide PCBs present many advantages, such as high operating temperature, extremely high flexibility, and durability [58]. Moreover, it is possible to design any shape due to their standardized and consolidated manufacturing process. Additionally, we chose to cover copper traces with gold using the Electroless Nickel Immersion Gold (ENIG) process as an additional service, as it protects the pads from oxidation and helps the adhesion of rGO-RI. Creating complex sensor shapes was then as simple as designing a standard PCB.

The preparation of pressure sensors onto rectangular (13 mm x 20 mm) and cross-shaped (20 mm diameter) flexible PCBs was carried out following a previously reported procedure [57] [59], with some modifications. Briefly, rGO-R1 active material was spray coated at 80°C onto the gold-coated side of the PCBs substrates. Before the spray coating, a customized shadow mask was applied to create an rGO-free surface to place electrical contacts. For both rectangular and cross-shaped geometries, 6 mL of rGO-R1 active material was spray-coated on the gold-coated side of the PCB substrates. After rGO-R1 deposition, the shadow mask was removed. Two of the obtained electrodes of analogous geometry were placed in a face-to-face configuration and fixed with polyimide (PI) tape (Fig. 2). Regarding the cross-shaped geometry, instead of using PI tape to build the sensor, the two sides were placed face-to-face and kept in place using a custom-made 3D-printed holder. Electrical contacts were then obtained by soldering copper wires on areas not coated (green and red arrows in Fig. 3). In the rectangle-shaped sensor, the current enters from one contact pad, passes from one side to the other, and exits from the other connection pad. In the cross-shaped one, the current path is a bit more complex. Concerning Fig. 3, the current follows a single path, starting from the red arrow, and is forced to pass through four different rGO-R1 covered pads and finally exit from the green arrow. The four rGO-R1 pads are strategically placed in series, increasing the total sensor resistance to acquire a more easily readable resistance value (1 to 10 Ohms).

E. Characterization

1) Deposition: Sensor performances were investigated as a function of the active material content and the resulting coverage of the PCB surface. The deposition of rGO-R1 coatings on the PCB surface was assessed through SEM analysis, as reported in Fig. 4. As shown in [57, Fig. 2(a)-i], based on the amount of rGO-R1 dispersion spray-coated on the PCB, we can achieve different degrees of coverage of the PCB surface (namely partial coverage, full coverage, and overload). Different surface coverage resulted in different performances in terms of durability and sensitivity.

2) Piezoresistivity: Fundamental characterization of the devices' performance was done on the rectangular sensors. Such performance was evaluated regarding pressure sensitivity and device durability upon application of cyclic stress. Such tests were carried out using a Mark-10 M7-025E digital force gauge mounted on a Mark-10 ESM-303E motorized test stand. The test setup had a round compression plate with a diameter of 1.15 cm. The sensitivity was assessed through static pressure tests, measuring the device's electrical resistivity when a static force was applied at 0.005 to 0.2 N (corresponding to a pressure range between 0.05 and 2 kPa). The resistivity was measured using a Keithley 2635B source meter. The durability of the devices was tested by cyclically applying a 0.5 kPa load and monitoring the change in electrical resistance over time using Labtracer. One-way analysis of variance (ANOVA) was used to evaluate statistical significance ($p < 0.05$). Error bars represent standard error of the mean, extrapolated from separate experiments on at least five different samples.

With increasing the active material content and coverage of the PCB surface, the sensitivity of the PCB devices increases gradually (Fig. 5a and Table I), going from 0.025 kPa^{-1} when partial coverage is achieved to 0.281 kPa^{-1} when full coverage is achieved. Further increase of the rGO-R1 content (overload) on the PCB surface results in a lower sensitivity of 0.137 kPa^{-1}. In all cases, the sensors also showed good linearity in the low-pressure range, as illustrated in Fig. 5b.

The PCB – rGO-R1 pressure sensors' robustness and stability were assessed through fatigue tests, carried out by applying a 0.5 kPa load in press-release cycles 1000 times (Fig. 5c and Table II). A significant loss in device sensitivity (more than 60%) is observed in the case of partially covered PCB surfaces and for overloaded devices. In both cases, the change in resistivity for the same applied load is accompanied by a

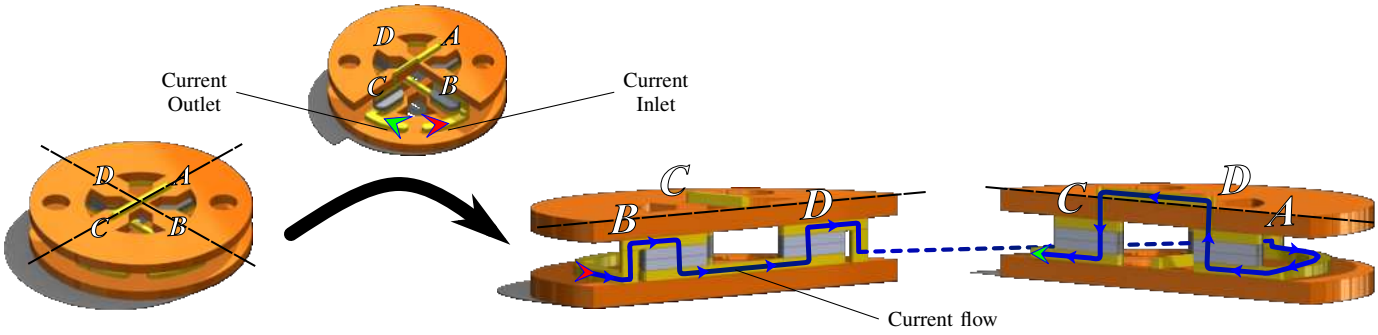

Fig. 3: Cross-sections of rectangular sensor. The current flow starts from the red arrow, passes through four different rGO-R1 pads in series, and finally exits from the green arrow.

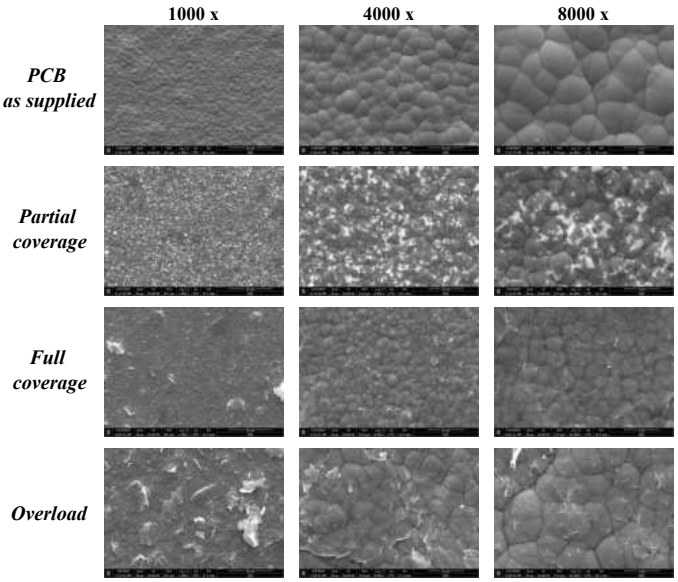

Fig. 4: SEM images for ITO-PET substrates before and after deposition of rGO-R1 in different proportions

degradation of the dynamic response to the mechanical stress, as can be observed from the change in the shape of the stress curves over time.

TABLE I: Sensitivity values calculated for different rGO-R1 based pressure sensors

Sample	Sensitivity (kPa^{-1})	R^2
PCB only	0.013	0.93
PCB + rGO-R1 (partial coverage)	0.025	0.91
PCB + rGO-R1 (full coverage)	0.281	0.98
PCB + rGO-R1 (overload)	0.137	0.99

Better stability is observed for the pressure sensors with fully covered PCB surface, with a good dynamic response to pressure load-unload even after 1000 cycles. Since the cross-shaped sensor needed its fixture to be kept in place, previously mentioned tests were executed only with the rectangular sensor. To properly mechanically characterize the cross-shaped sensor, another kind of tests were carried out closer to the final application.

TABLE II: Pressure sensitivity at 0.5 kPa for PCB-rGO R1 devices before and after fatigue test

Sensor	R/R0 at 0.5 kPa	R/R0 after 1000 cycles	Sensitivity loss
PCB (no active material)	0.0038 (± 0.0003)	0.0038 (± 0.0002)	N.A.
PCB + rGO-R1 (partial coverage)	0.0157 (± 0.0071)	0.0059 (± 0.0011)	-62%
PCB + rGO-R1 (full coverage)	0.0335 (± 0.0023)	0.0250 (± 0.0031)	-25%
PCB + rGO-R1 (overload)	0.0647 (± 0.0040)	0.0250 (± 0.0039)	-61%

3) Mechanical: Sensors were characterized mechanically to assess their performance in terms of the correlation between the displacement of the graphene-based diaphragm and the voltage output of the system. Tests on rectangular and circular-shaped sensors evaluated the behavior and differences between variants.

Figure 6 shows the experimental setup whose main components are listed below:

- *Vibration test system*; the main equipment of the experimental set-up is the TIRA TV 51120 vibration test system, which consists of a vibration exciter (shaker) and its amplifier to generate and modulate the oscillatory stimulus respectively. The amplifier was fed with a waveform generated with a VirtualBench from National Instruments.
- *Shaker-sensor interface*: the moving coil of the shaker was coupled with the sensor through a slender rod, called a stinger, to transmit the oscillatory stimulus. One extremity of the stinger is clamped on the moving coil while the other extremity pushes the sensor's membrane. The free extremity of the stinger ends with a 3D-printed tip to ensure a precise application of the oscillating motion to the sensing element. Various tips were designed that allow optimal adaptation to different shapes of sensor variants.
- *Sensor's support*: different 3D-printed housings were designed for the rectangular and circular sensors to ensure stability and proper positioning during the experiments. These housings were mounted on a metal stand, which, in turn, was attached to the working table with screws.

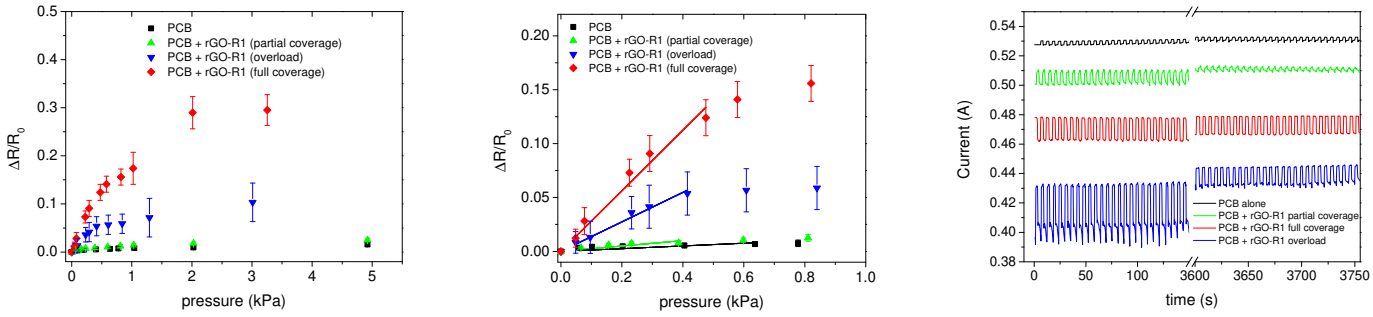

(a) (b) (c)

Fig. 5: (a) Relative resistance as a function of the applied pressure for different devices. (b) Sensitivity in the low-pressure range regime. (c) Fatigue tests under cycling application of 0.5 kPa load over time.

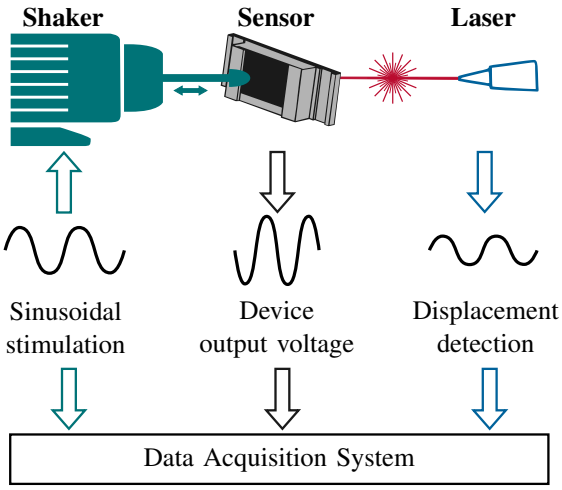

Fig. 6: Experimental set-up for the mechanical characterization of the sensors. The shaker applies a sinusoidal vibration transmitted to the sensor's center through a stinger. A vibrometer (laser) detects displacements of the diaphragm. A data acquisition system collects the data. The experiment repeats for both the rectangular and the circular sensors.

- *Laser Vibrometer*: the displacement of the sensors was precisely measured with a Laser Doppler Vibrometer (LDV). Because the LDV is a non-contact measurement system, the membrane velocity was accurately measured without interfering with surface motion. The velocity was then converted to displacement by trapezoidal numerical integration.
- *Data acquisition system*: the velocity measured by the LVD, voltage, and current feeding the shaker were collected by an acquisition card, plotted online for immediate checking, and stored on the hard disk by in-house software. An experimental protocol was designed to recreate a simplified version of a pressure signal typical of the target application. For this purpose, the characteristics of the oscillatory stimulus were set up as shown below:
  - Sine wave stimulation
  - 1 Hz frequency (similar to the pulse signal range)
  - Low shaker voltage amplitudes to generate small displacements (of the order of hundreds of micrometers)
  - Various voltage amplitudes for different tests
  - Application of a displacement offset to reproduce static pressure, which is always present during pulse acquisitions

The mechanical characterization was carried out on both rectangular and cross-shaped sensors, setting sinusoidal stimuli of different amplitudes and acquiring the resulting voltage output from the device. The amplitude of the stimulation was progressively incremented until a plateau was reached, as shown in Fig.7. While the rectangular sensor showed a steeper curve for lower displacements, the circular cross-shaped sensor proved better performance for higher ranges.

For each acquisition, the voltage output of the devices was compared with the displacement curve derived from the integration of the velocity data obtained from the vibrometer. The output signals exhibit a counter-phase relationship with the sinusoidal displacement. This finding is consistent with the predicted behavior, indicating a resistance decrease as pressure increases.

The rectangular sensor produces quasi-sinusoidal voltage outputs for small displacements, consistent with the input displacement. However, slight distortions around the peaks are observed for larger displacements; see Fig. 7a. To quantify this assumption, the signal-to-noise ratio (SNR) was calculated for different displacement amplitudes (75 µm and 182 µm). These values were chosen to have a range of approximately 100 µm backwards from the start of the plateau. The SNR resulted being:

- $SNR_{75\,\mu m} \approx 21$ dB
- $SNR_{182\,\mu m} \approx 20$ dB

In contrast, the circular sensor consistently exhibits the expected behavior for any value of applied displacement amplitude as shown in Fig. 7b for smaller and larger displacement amplitudes, respectively. The response of the circular sensor is significantly closer to the desired characteristics than the rectangular sensor. With the same logic as for the rectangular sensor, the signal corresponding to 195 µm and 300 µm was taken into account. It results that higher displacements produce higher SNRs:

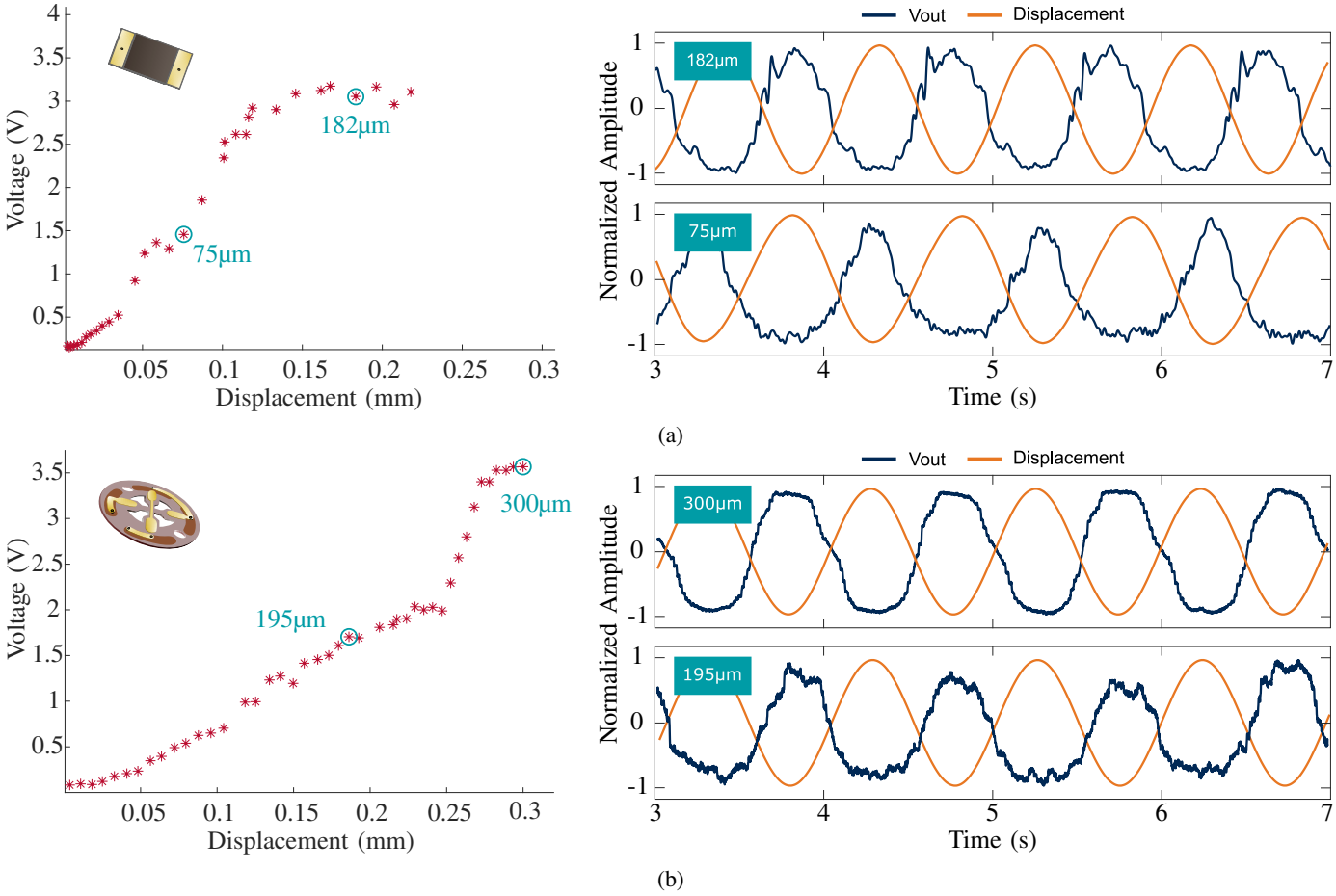

Fig. 7: Relationship between the output voltage of the device and the displacements (red) obtained during the mechanical characterization of the rectangular (a) and circular (b) sensors. The tests were conducted by applying sinusoidal stimuli with progressively increments of amplitude until a plateau was reached. The plots on the right show the system's output voltage response (blue) compared to the sensor displacements (orange), both normalized in the figure. These graphs are displayed for two displacement amplitude values for each sensor (75 µm and 182 µm for the rectangular sensor, 195 µm and 300 µm).

- $\text{SNR}_{195\,\mu\text{m}} \approx 19$ dB
- $\text{SNR}_{300\,\mu\text{m}} \approx 25$ dB

III. Reading System

Dealing with small resistance variations of the order of tens of mΩ requires properly designing a sensitive conditioning circuit to convert tiny pressure inputs into readable voltage outputs. Moreover, piezoresistivity changes over time depending on environmental conditions, such as temperature and humidity, or loss of sensitivity due to structural defects that can occur across the sensor's lifespan [60]–[62]. For this study, we have designed and developed a readout circuit whose core relies on a smart current-based Wheatstone bridge. Fig. 8 provides an overview of the proposed readout circuit.

The circuit first transforms the bridge output current, which is proportional to the applied pressure, into a raw voltage signal and then processes it using analog blocks to make it ready for reading. An STM32 microcontroller unit (MCU) converts the analog output into digital data using an analog-to-digital converter (ADC) and sends it externally to a PC via USB. As displayed in Fig. 8a, the circuitry splits into three different printed-circuit-boards (PCB). The circular PCB matches the sensor's dimensions and connects to its pads through the use of spring-loaded connectors (Fig. 8b); moreover, it contains the first stages of the conditioning circuit, including the Wheatstone bridge. The raw signal travels via wires to a second PCB (main board), which further processes it. The main board physically and electrically attaches to an SF2W pyboard D-series, which integrates the MCU responsible for managing the acquisition and control of the entire circuit.

The following sections present more detailed descriptions of the various stages of the circuitry.

A. Current based Wheatstone bridge

Fig. 8c shows an high-level representation of the readout schematic. For this study, a current-based Wheatstone bridge configuration, based on the circuit exploited in [63], was adopted to readout the resistance changes of the sensor. This configuration proved high accuracy ($< 0.001\,\text{m}\Omega$) due to its capability of self-balancing. As widely recognized, the typical resistive Wheatstone bridge comprises four distinct resistors, which, when equal, maintain the bridge's balance. In our implementation (Fig. 9), the sensor (indicated as R_S), placed

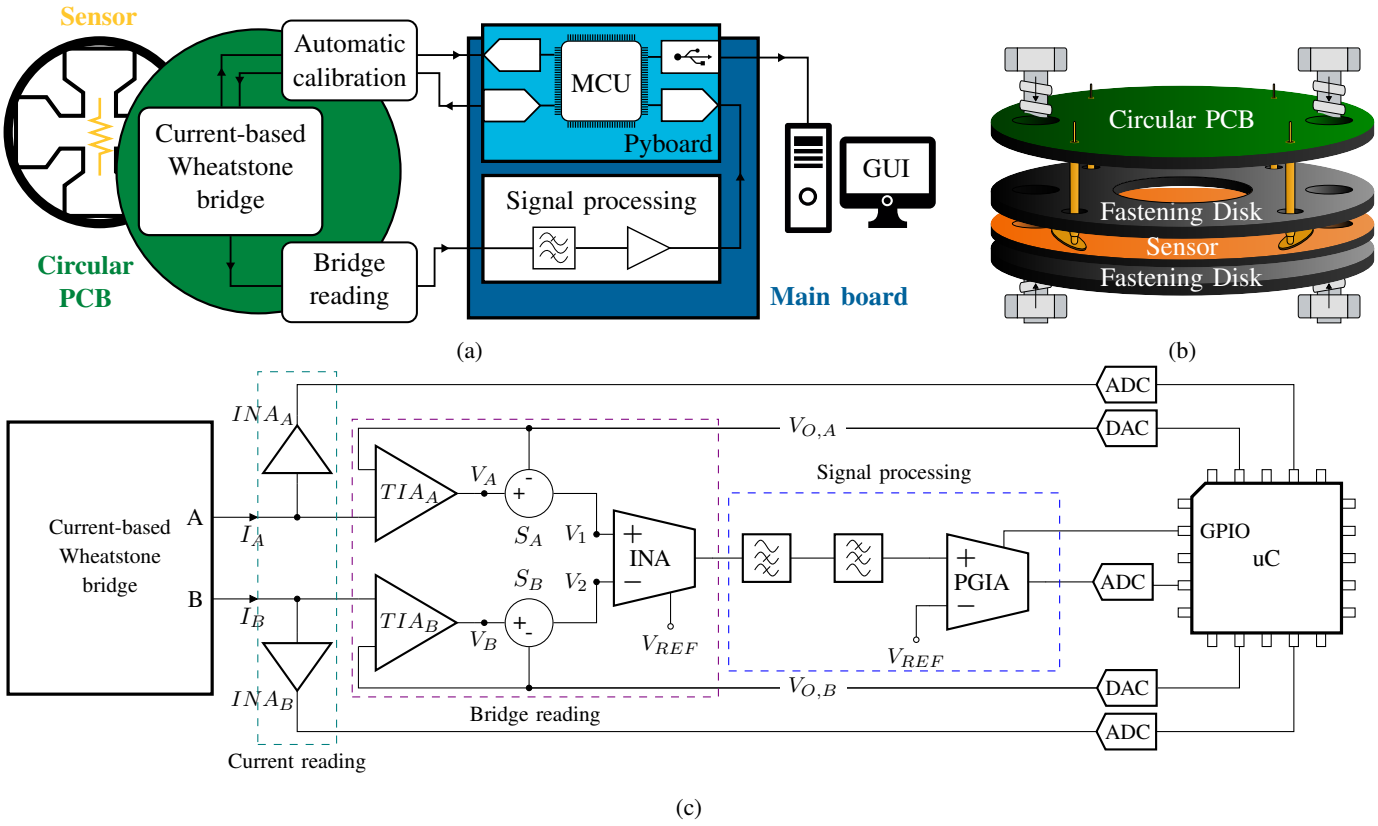

Fig. 8: (a) Readout circuit representation. The circuit is shared by three different PCBs: the circular PCB (green) directly connects to the pressure sensor, detects and converts its resistivity variations into a voltage signal; the main board (dark blue) contains the signal processing stage and is fixed to a pyboard D-series (light blue). (b) Interface between the sensor and the circular PCB. Two 3D-printed disks keep the sensor steady. Four spring-loaded soldered to the circular PCB contact the sensor's conductive pads, performing the electrical connection. Two screws fasten the whole sensing system.(c) Block diagram of conditioning circuit. Dashed boxes surround different functional sections of the circuit.

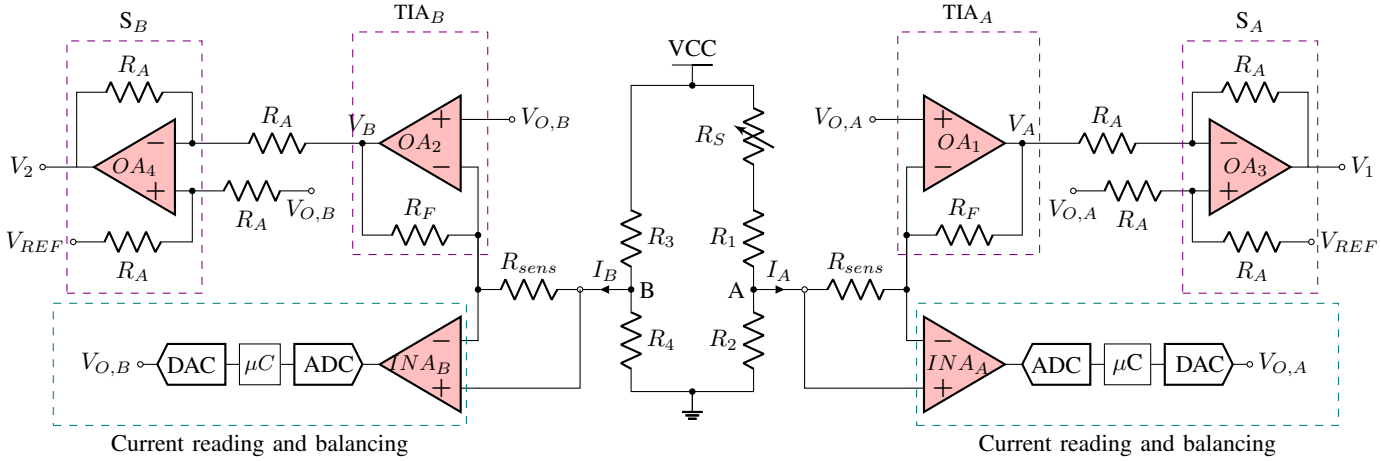

Fig. 9: Schematic of the adopted current-based Wheatstone bridge, with a voltage mode balancing configuration based on the use of two operational amplifiers [63]. During the self-balancing phase, the current is measured by acquiring the voltage fall through R_{sense}. A microcontroller (μC) calculates and sets one offset value for each side of the Wheatstone Bridge ($V_{O,A}$ and $V_{O,B}$) in order to minimize the current. During the acquisition phase, the output currents from the Wheatstone bridge (I_A and I_B) are converted into voltages with transimpedance amplifiers (TIA_A and TIA_B). $V_{O,A}$ and $V_{O,B}$ are finally removed from the signal by S_A and S_B, to not affect the output signal from the balancing offset.

in series with one of the four resistors (R_1), serves as the sole variable element in the configuration. Thus, a variation of the sensor's resistance induces imbalance to the Wheatstone bridge, with a consequent generation of non-null output voltage (V_{OUT}) and currents (I_A and I_B) whose difference (I_{OUT}) is proportional to the sensor's resistance variation. In a current-based approach, I_{OUT} is the conditioned output signal, and it can be calculated as:

$$\begin{aligned} I_{OUT} &= I_B - I_A \\ &= \frac{V_{CC}}{2} \frac{(R_1 + R_S)R_2(R_4 - R_3) - R_3R_4(R_2 - (R_1 + R_S))}{(R_1 + Rs)R_2R_3R_4}. \end{aligned} \tag{1}$$

If $R_0 = R_1 = R_2 = R_3 = R_4$, the previous formula can be simplified as:

$$I_{OUT} = \frac{V_{CC}}{2} \frac{R_S}{R_0(R_0 + R_S)}. \tag{2}$$

The sensitivity of a conditioning circuit can be defined as the derivative of the output variable concerning the input one, as shown in (3). For the case under evaluation, if $R_0 >> R_S$ it is possible to approximate the calculation as following:

$$\begin{aligned} S_{C.Co} &= \frac{\partial I_{OUT}}{\partial R_S} \\ &= \frac{V_{CC}}{2} \frac{R_0^2 - R_S R_0}{(R_0(R_0 + R_S))^2} \\ &\approx \frac{V_{CC}}{2} \frac{1}{R_0^2}. \end{aligned} \tag{3}$$

1) Bridge's automatic balancing system : The self-balancing system was designed starting from two operational amplifiers (OAs), each connected to the corresponding Wheatstone bridge node (A or B) through their inverting pins. Concerning Fig. 9, by applying a predefined offset voltage value (V_{OFF}) to the non-inverting terminal, voltage levels are forced to the A and B output nodes of the bridge to find a balance to null the two output currents I_A and I_B. This strategy ensures that even small changes in resistance within the bridge due to external factors like temperature fluctuations or drifts over time do not significantly impact on the output signal, leading to a more accurate measurement.

The determination of the offset values applied to the nodes A and B ($V_{O,A}$ and $V_{O,B}$, respectively) is automatically performed by the MCU, programmed to read the value of the output currents and generate the proper voltage offset to send to the OAs. To execute the current measurement, an instrumentation amplifier (INA) readouts and amplifies the voltage fall caused by the passage of the current through a resistor (R_{sense}), as shown by Fig. 9. The INA's output signal is transmitted to the MCU, where a dedicated "zeroing" algorithm takes charge.

2) Bridge reading: With the completion of the calibration, the circuit is ready to perform the measurement, with I_A and I_B, which predominantly reflect the sole pressure variations. The OAs employed for the bridge balancing play a dual role, also serving as transimpedance amplifiers (TIAs) to convert the current signal into a voltage signal. The TIA output signal is determined by the value of the feedback resistor R_F:

$$\begin{aligned} V_A &= -I_A R_F + V_{O,A}, \\ V_B &= -I_B R_F + V_{O,B}. \end{aligned} \tag{4}$$

The previously applied offset is subsequently eliminated from the signal for both branches not to affect the measurement. This is accomplished by integrating a unity-gain inverting operational amplifier (represented as S_A and S_B in Fig. 8c) within the conditioning chain. This amplifier subtracts the V_{OFF} value from the TIA output signal, nullifying the offset effect. Moreover, this stage shifts the output voltage to a predetermined reference voltage value, set at half of the voltage supply (V_{CC}) as shown in (5):

$$\begin{aligned} V_1 &= -V_A + V_{O,A} + V_{REF} \\ &= I_A R_F + \frac{V_{CC}}{2}, \\ V_2 &= -V_B + V_{O,B} + V_{REF} \\ &= I_B R_F + \frac{V_{CC}}{2}. \end{aligned} \tag{5}$$

Additionally, an INA is inserted to subtract and amplify the two resultant signals obtained from the left and right branches of the Wheatstone bridge:

$$\begin{aligned} V_{OUT} &= G(V_2 - V_1) + \frac{V_{CC}}{2} \\ &= G R_F (I_B - I_A) + \frac{V_{CC}}{2} \\ &= G R_F I_{OUT} + \frac{V_{CC}}{2}, \end{aligned} \tag{6}$$

where 'G' is the gain of the INA, calculable as:

$$G = 1 + \frac{100k\Omega}{R_g} \tag{7}$$

From (6) and (2) it is possible to determine the value of R_S:

$$R_S = \frac{2V_{OUT}R_0^2 - V_{CC}R_0^2}{V_{CC}R_0 - 2V_{OUT}R_0 + V_{CC}GR_F}, \tag{8}$$

where 'V_{CC}', 'R_0', 'G', and 'R_F' are known and 'V_{OUT}' is measured.

The circuit which has just been described is mounted on the circular PCB. The signal is sent to the main board via wires, where it will be further processed.

B. Analog signal processing

The hardware processing stage commences with two third-order Sallen-Key filters: high-pass (HPF) and low-pass (LPF). Specifically, each filter is created by the combination of first-order and second-order filters, each characterized by its cut-off frequency. Whereas the HPF attenuates the continuous and low-frequency components, the LPF reduces high-frequency noise. The characteristics of the signal under study guide the choice of the two cut-off frequencies. For this paper's application focus, the bandwidth of interest spans from a fraction of hertz to a few tens of hertz. Consequently, cut-off frequencies of 0.1 Hz and 20 Hz have been picked up.

The last analog stage of the conditioning circuit is a programmable-gain instrumentation amplifier (PGIA) made of

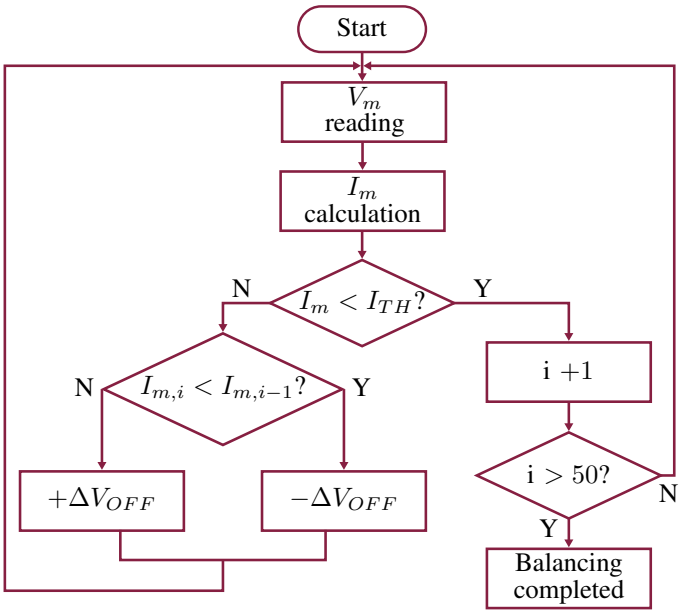

Fig. 10: Workflow of the automatic Wheatstone bridge balancing algorithm.

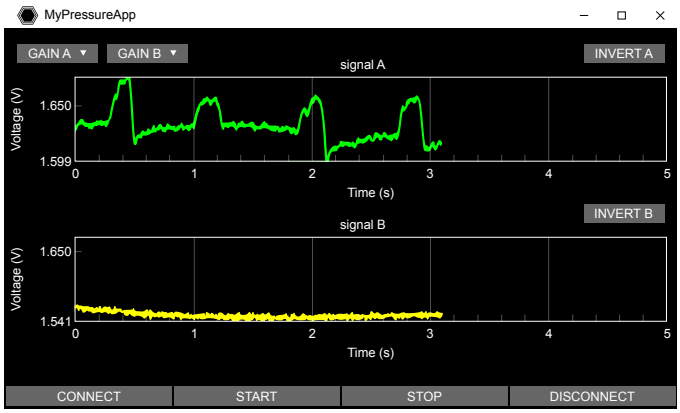

Fig. 11: Layout of the implemented GUI application.

an INA and a multiplexer (MUX). The INA's gain is set by the value of an external resistor, as already shown in equation (7), which can be connected to specific amplifier terminals. In this system, eight different resistors have been used to set equal gains. By doing so, it is possible to adapt the signal dynamically to the ADCs, depending on the application and the magnitude of the pressure variation. This solution enhances the device's versatility, making it suitable for performing measurements with different working ranges. The resistors are connected to the INA through a MUX controlled by the MCU, which closes the switch corresponding to the selected gain.

The output analog signal is lastly sent to the MCU board (pyboard D-series) and converted into digital data with an ADC.

IV. Firmware

We implemented the firmware in Micropython for the pyboard, based on an STM32 MCU, which performs the different tasks in charge of the pressure sensing system management. The script integrates different data acquisition and transmission functions, serial communication with the user, hardware component programming, and bridge balancing.

The firmware starts by configuring various components, such as ADCs, DACs, SPI, timers and USB.

The first scheduled routine is the "current zeroing algorithm" for the automatic Wheatstone bridge balancing (Fig. 10). The two offsets to apply to the non-inverting inputs of the TIAs, are both initialized as $V_{CC}/2$. To generate $V_{O,A}$ and $V_{O,B}$, the MCU programs two DACs integrated into the circular PCB via SPI communication. If I_m exceeds I_{TH}, the MCU adjusts $V_{O,A}$ in steps of ΔV_{OFF} to decrease I_m with respect to the previously measured value, and the algorithm starts over. When I_m turns lower than I_{TH}, a counter increments and a new iteration commences. If (I_m) remains below (I_{TH}) for 50 consecutive iterations (a reasonable compromise between time and accuracy), the right branch achieves balance, and the final $(V_{O,A})$ value is set. If not, the counter resets to zero, causing the process to recommence from the beginning. The whole algorithm repeats for the left branch of the Wheatstone bridge.

After the calibration is completed, the system is ready to start the acquisition of the signal. The data collection begins when the user sends the corresponding command to the MCU from the PC via USB. An ADC converts the analog signal into digital at a sampling frequency of 1 kHz to satisfy the bandwidth requirements imposed by the application of interest. The data are finally transmitted to the laptop via USB.

V. Graphical User Interface

We also developed a graphical user interface (GUI) application with the Python programming language, intending to acquire the data and visualize them in real-time (Fig. 11). The software is primarily designed to diagnose biomedical signals but can be extended to other applications.

The layout was defined using the Kivy framework, which enables the generation of screens and graphical widgets, such as control buttons or drop-down menus. The interaction with these widgets allows us to send commands to the MCU via USB and set different parameters. The screen splits into two distinguished graphs, allowing the simultaneous plotting of two signals, which is important for simultaneously monitoring the pulse wave signal from two different sites.

The communication with the serial port begins by clicking the "Connect" button, which connects to the device and starts the automatic calibration of the Wheatstone bridge. Once calibrated, a "Start" button enables digital signal acquisition. Samples are loaded into a buffer, saved to a text file, and displayed on a digital screen. Every 5 seconds, the input buffer updates with new data, auto-scaling the y-axis for proper visualization. A drop-down menu allows the user to select the gain for the PGIA. Finally, the "Disconnect" button stops the real-time plotting, closes the serial communication, and turns off the GUI.

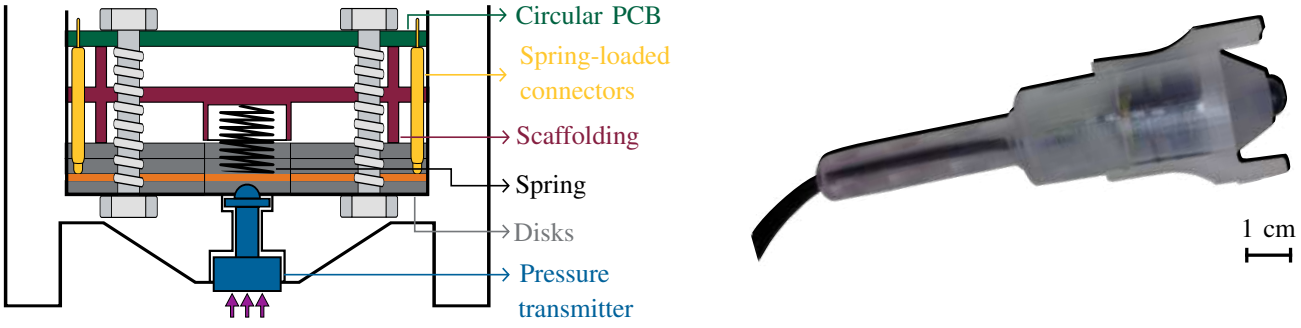

(a) (b)

Fig. 12: (a) Illustration of a section of the pressure sensor holding system's tip: the 3D-printed pen (white) homes the sensing system, which is composed of the sensor (orange) kept steady by two plastic disks (dark grey), the circular PCB (spring-loaded connectors (yellow), a spring (black), screws and the supporting scaffold (red). (b) Picture of the pen-shaped holder.

VI. Application

This section presents a series of tests, conducted with the cross-shaped sensor, to showcase the sensor's effectiveness and translate the promising characterization results into practical applications. In this perspective, no comparisons with the state-of-the-art are performed since such preliminary tests have the unique purpose of demonstrating sensor potential in future biomedical device implementation. Pressure sensors have found applications across various domains, ranging from healthcare and biomedical research to industrial and consumer electronics. In this context, our primary focus revolves around the real-time screening of the arterial pulse, being part of research activities of our research group [64]–[71]. Arterial pulse wave analysis can be performed to assess arterial stiffness and overall cardiovascular function by calculating the PWV.

A. Mechanical System

In pursuit of creating a user-friendly device to perform the acquisition of the arterial pulse wave, we have designed a mechanical system tailored for this specific application (Fig. 12). While initial testing with medical professionals indicates promising results, further studies are warranted to quantify the system's accuracy using established metrics. The sensor's case main structure is a pen-like shape holder intended for housing the device and guaranteeing comfortable handling by an operator. At one extremity, a fastening system allows for the interchangeability of different tips, constituting the interface between the pressure source and the sensor. In such a manner, the device offers adaptability to the anatomical characteristics of the artery and the surrounding tissues. The user can select one of the different available tips; each designed best to accommodate the anatomical features of the site under evaluation, and easily assemble it on the holder. The pen's tip contains a pressure-transmitting system consisting of two integral components: a skin-side cylinder and a sensor-side tip. The dimensions of the skin-side cylinder are thought to match the diameter of the artery, ensuring precise and consistent contact. The sensor-side tip is positioned to apply pressure lengthwise at the center of the pressure sensor. The two components are affixed to the pen's tip and securely bonded using a resistant adhesive. To further enhance the usability and effectiveness of the device, the pen's tip presents two "wings" on the skin side. These wings serve as support to lay down the holder to the skin comfortably and create an outlet to reduce the static pressure value acting on the sensor. The sensor is inserted within the pen into a "pocket" to maintain stability during the measurements. The use of spring-loaded pins electrically interfaces the sensor and the circular board. To guarantee a reliable connection, we've incorporated two 3D-printed disks, positioning them on either side of the sensor. These disks are affixed to the PCB through the use of four screws, thereby establishing a robust and enduring fastening. After being pressed, we observed a slow and incomplete elastic recovery, which in turn impacted the system's sensitivity during pulse wave acquisitions. To rectify this problem, a soft spring was integrated to improve the sensor's elastic properties without significantly affecting the measurement accuracy. This spring was positioned within a dedicated guide, engineered to create a contact only during the sensor's bending. This guide is part of a dual-role structure: as well as keeping the spring steady in a perpendicular and centered way with respect to the sensor's cross, it works as a"scaffold" for the device, imposing a fixed distance between the two components. By adopting this solution, the forces applied to the sensor are balanced, including those from the spring-loaded connectors and the spring's compression forces.

The whole mechanical system is illustrated in Fig. 12a. For the production of the components (holder, tips, disks and scaffold) we employed a 3D printer based on the stereolithography technology.

B. Application Examples

To roughly assess its functionality, one of the first trials involved the application of quick and controlled clicks with the index finger to the tip of the pen holder, housing the sensor. By doing so, we could evaluate its ability to register rapid pressure changes and promptly relay this data to the system for analysis.

Finally, we performed trials for acquiring physiological arterial pulse signals. To this end, a trained healthcare professional utilized our pressure sensing system to collect pulse wave signals from the carotid and femoral arteries. We used the

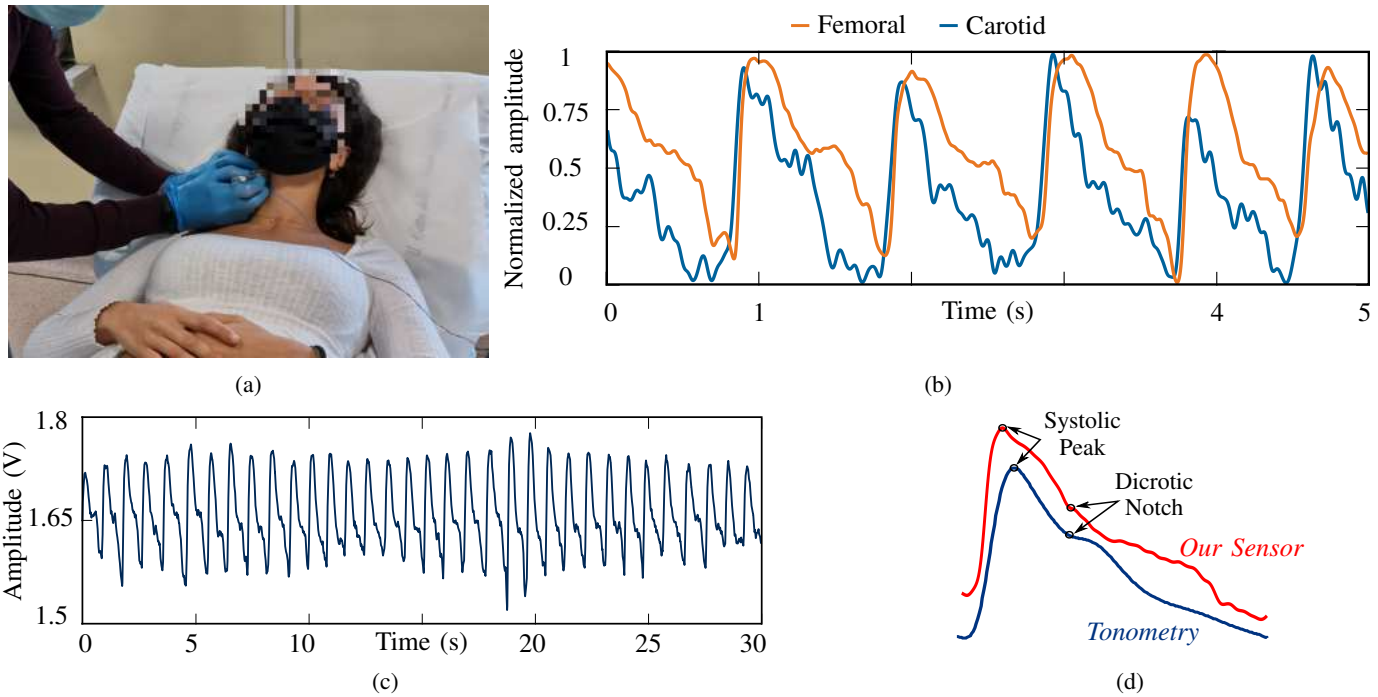

Fig. 13: (a) Pictures of a testing session during the acquisition of the pulse wave signal from the carotid artery. (b) Five seconds of simultaneous acquisition of carotid (blue) and femoral (orange) pulse wave signals using the developed device. (c) Pressure signal taken from the femoral artery of a volunteer during a one-minute acquisition.(d) Shape comparison between carotid pulses obtained by our sensor and reference technique.

mechanical holder described earlier to ensure precision and comfort during measurements. This preliminary testing phase included a small and restricted group of volunteers. It aimed to validate, as a proof-of-concept, the device to prove its suitability for upcoming actual clinical trials.

Fig. 13a display a photograph of the experimental set-up, with the operator using the pen holder to position the tips at the carotid site of interest.

To demonstrate the stability and reliability of the system, we conducted a session to gather data from a single site for a prolonged time. Fig. 13c presents a 30-seconds track of femoral pulse waves. The system could continuously record pulses with physiological shapes throughout the entire duration, with no performance degradation. To prove the quality of the acquired physiological signals, we calculated the SNR of more than 100 pulse waves and averaged the results, obtaining an SNR of 23.5 dB. This result is consistent with the SNR obtained during the mechanical characterization (section II-E.3).

Finally, we accomplished simultaneous acquisitions from both the carotid and femoral arteries, aiming to validate the system's intended application. We meticulously set up the experimental environment adopting the clinical conditions carried on at a hospital structure. The operator carefully positioned the two holders at the dedicated spots on the volunteers' skin's surface. During the trials, the professional received visual feedback via the developed GUI. In the post-processing phase, we superimposed the two signals for comparison. An example of the results is presented in Fig. 13b. As noticeable from the rising edges, the femoral pulse waves exhibited a slight time shift with respect to the carotid pulses, illustrating the expected delay in pressure transmission. This delay is known as Pulse Transit Time (PTT), an important parameter for Pulse Wave Velocity (PWV) estimation. These outcomes underscore the device's suitability for further clinical evaluations and applications, affirming its potential in medicine.

VII. Conclusions

This paper presented the design, fabrication, and characterization of a novel integrated rGO-based pressure sensor, suitable for various biomedical applications. The sensor is a thin layer of rGO-R1, a graphene derivative with enhanced piezoresistive properties, deposited on a flexible PCB substrate. The sensor exhibits high sensitivity, wide detection range, response time of 41 ms, which is perfectly adapted to pulse monitoring via biomedical pressure sensors, and good stability under cyclic loading. We have also developed a smart current-based Wheatstone bridge circuit to condition the sensor output and firmware to control the bridge balancing and data acquisition. Furthermore, we have designed a mechanical system to adapt the sensor to different anatomical sites and to improve its elastic recovery. We have demonstrated the functionality of our sensor by acquiring physiological signals from the carotid and femoral arteries of volunteers, showing its ability to capture, according to expert physicians judge, the pulse waveforms strongly comparable to the one recorded in clinical practice with applanation tonometry techniques. This enables to measure the pulse transit time, an important parameter for estimating the pulse wave velocity and arterial stiffness. However, our sensor is not limited to this specific

application, and can be easily extended to other domains where pressure sensing is required. Our sensor offers a low-cost, flexible, and user-friendly solution for non-invasive biomedical monitoring and diagnosis.

ACKNOWLEDGMENTS

The authors would like to sincerely thank Professor Andrea De Marcellis for his support on the current-based Weathstone bridge development. P.S. acknowledges funding from the European Union's Horizon Europe research and innovation programme through the project HYPERSONIC (GA-101129613) and ANR through the Interdisciplinary Thematic Institute SysChem via the IdEx Unistra (ANR-10-IDEX-0002) within the program Investissement d'Avenir, the Foundation Jean-Marie Lehn and the Institut Universitaire de France (IUF).

REFERENCES

[1] J. Hu, G. Dun, X. Geng, J. Chen, X. Wu, and T.-L. Ren, "Recent progress in flexible micro-pressure sensors for wearable health monitoring," *Nanoscale Advances*, vol. 5, no. 12, pp. 3131–3145, 2023.

[2] Y. Duan, S. He, J. Wu, B. Su, and Y. Wang, "Recent progress in flexible pressure sensor arrays," *Nanomaterials*, vol. 12, no. 14, p. 2495, 2022.

[3] C. Xu, J. Chen, Z. Zhu, M. Liu, R. Lan, X. Chen, W. Tang, Y. Zhang, and H. Li, "Flexible pressure sensors in human–machine interface applications," *Small*, vol. 20, no. 15, p. 2306655, 2024.

[4] A. Milan, G. Zocaro, D. Leone, F. Tosello, I. Buraioli, D. Schiavone, and F. Veglio, "Current assessment of pulse wave velocity: comprehensive review of validation studies," *Journal of Hypertension*, vol. 37, no. 8, pp. 1547–1557, Aug 2019.

[5] C. B. Huang, Y. Yao, V. Montes-García, M. A. Stoeckel, M. V. Holst, A. Ciesielski, and P. Samorì, "Highly sensitive strain sensors based on molecules–gold nanoparticles networks for high-resolution human pulse analysis," *Small*, vol. 17, no. 8, p. 2007593, Feb 2021.

[6] K. Meng, X. Xiao, W. Wei, G. Chen, A. Nashalian, S. Shen, X. Xiao, and J. Chen, "Wearable pressure sensors for pulse wave monitoring," *Advanced Materials*, vol. 34, no. 21, p. 2109357, May 2022.

[7] K. Roy, S. K. Ghosh, A. Sultana, S. Garain, M. Xie, C. R. Bowen, K. Henkel, D. Schmeißer, and D. Mandal, "A self-powered wearable pressure sensor and pyroelectric breathing sensor based on go interfaced pvdf nanofibers," *ACS Applied Nano Materials*, vol. 2, no. 4, pp. 2013–2025, Apr 2019.

[8] J. Zhong, Z. Li, M. Takakuwa, D. Inoue, D. Hashizume, Z. Jiang, Y. Shi, L. Ou, M. O. G. Nayeem, S. Umezu, K. Fukuda, and T. Someya, "Smart face mask based on an ultrathin pressure sensor for wireless monitoring of breath conditions," *Advanced Materials*, vol. 34, no. 6, p. 2107758, Feb 2022.

[9] Y. Xiong, Y. Shen, L. Tian, Y. Hu, P. Zhu, R. Sun, and C. P. Wong, "A flexible, ultra-highly sensitive and stable capacitive pressure sensor with convex microarrays for motion and health monitoring," *Nano Energy*, vol. 70, p. 104436, Apr 2020.

[10] M. Bai, Y. Zhai, F. Liu, Y. Wang, and S. Luo, "Stretchable graphene thin film enabled yarn sensors with tunable piezoresistivity for human motion monitoring," *Scientific Reports*, vol. 9, no. 1, p. 18644, Dec 2019.

[11] L. Q. Tao, K. N. Zhang, H. Tian, Y. Liu, D. Y. Wang, Y. Q. Chen, Y. Yang, and T. L. Ren, "Graphene-paper pressure sensor for detecting human motions," *ACS Nano*, vol. 11, no. 9, pp. 8790–8795, Sep 2017.

[12] X. Fu, J. Li, D. Li, L. Zhao, Z. Yuan, V. Shulga, W. Han, and L. Wang, "Mxene/zif-67/pan nanofiber film for ultra-sensitive pressure sensors," *ACS Applied Materials Interfaces*, vol. 14, no. 10, pp. 12 367–12 374, Mar 2022.

[13] K. H. Ha, W. Zhang, H. Jang, S. Kang, L. Wang, P. Tan, H. Hwang, and N. Lu, "Highly sensitive capacitive pressure sensors over a wide pressure range enabled by the hybrid responses of a highly porous nanocomposite," *Advanced Materials*, vol. 33, no. 48, p. 2103320, Sep 2021.

[14] S. Song, C. Zhang, W. Li, J. Wang, P. Rao, J. Wang, T. Li, and Y. Zhang, "Bioinspired engineering of gradient and hierarchical architecture into pressure sensors toward high sensitivity within ultra-broad working range," *Nano Energy*, vol. 100, p. 107513, Sep 2022.

[15] G. Zhu, H. Dai, Y. Yao, W. Tang, J. Shi, J. Yang, and L. Zhu, "3d printed skin-inspired flexible pressure sensor with gradient porous structure for tunable high sensitivity and wide linearity range," *Advanced Materials Technologies*, vol. 7, no. 7, p. 2101239, Dec 2021.

[16] O. Legendre, H. Bertin, O. Garel, M. Zhang, H. Mathias, S. Mergherbi, J. Juillard, and F. Mailly, "High-resolution micro-pirani pressure sensor with transient response processing and time-constant evaluation," *IEEE Sensors Journal*, vol. 12, no. 10, pp. 3090–3097, Oct 2012.

[17] J. Chen, J. Zhang, J. Hu, N. Luo, F. Sun, H. Venkatesan, N. Zhao, and Y. Zhang, "Ultrafast-response/recovery flexible piezoresistive sensors with dna-like double helix yarns for epidermal pulse monitoring," *Advanced Materials*, vol. 34, no. 2, p. 2104313, Nov 2021.

[18] J. Oh, J. O. Kim, Y. Kim, H. B. Choi, J. C. Yang, S. Lee, M. Pyatykh, J. Kim, J. Sim, and S. Park, "Highly uniform and low hysteresis piezoresistive pressure sensors based on chemical grafting of polypyrrole on elastomer template with uniform pore size," *Small*, vol. 15, no. 33, p. 1901744, Jun 2019.

[19] F. Xu, X. Li, Y. Shi, L. Li, W. Wang, L. He, and R. Liu, "Recent developments for flexible pressure sensors: a review," *Micromachines*, vol. 9, no. 11, p. 580, Nov 2018.

[20] J. Lee, J. Kim, Y. Shin, and I. Jung, "Ultra-robust wide-range pressure sensor with fast response based on polyurethane foam doubly coated with conformal silicone rubber and cnt/tpu nanocomposites islands," *Composites Part B: Engineering*, vol. 177, p. 107364, Nov 2019.

[21] T. Chen, S. H. Zhang, Q. H. Lin, M. J. Wang, Z. Yang, Y. L. Zhang, F. X. Wang, and L. N. Sun, "Highly sensitive and wide-detection range pressure sensor constructed on a hierarchical-structured conductive fabric as a human–machine interface," *Nanoscale*, vol. 12, no. 41, pp. 21 271–21 279, 2020.

[22] N. Bai, L. Wang, Y. Xue, Y. Wang, X. Hou, G. Li, Y. Zhang, M. Cai, L. Zhao, F. Guan, X. Wei, and C. F. Guo, "Graded interlocks for iontronic pressure sensors with high sensitivity and high linearity over a broad range," *ACS Nano*, vol. 16, no. 3, pp. 4338–4347, Mar 2022.

[23] Z. Shi, L. Meng, X. Shi, H. Li, J. Zhang, Q. Sun, X. Liu, J. Chen, and S. Liu, "Morphological engineering of sensing materials for flexible pressure sensors and artificial intelligence applications," *Nano-Micro Letters*, vol. 14, no. 1, p. 141, Jul 2022.

[24] Bijender and A. Kumar, "Recent progress in the fabrication and applications of flexible capacitive and resistive pressure sensors," *Sensors and Actuators A: Physical*, vol. 344, p. 113770, Nov 2022.

[25] J. Huang, G. Xie, Q. Wei, Y. Su, X. Xu, and Y. Jiang, "Degradable mxene-doped polylactic acid textiles for wearable biomonitoring," *ACS Applied Materials Interfaces*, vol. 15, no. 4, pp. 5600–5607, 2022.

[26] H. Pan, G. Chen, Y. Chen, A. Di Carlo, M. Mayer, S. Shen, C. Chen, W. Li, S. Subramaniam, H. Huang, and H. Tai, "Biodegradable cotton fiber-based piezoresistive textiles for wearable biomonitoring," *Biosensors and Bioelectronics*, vol. 222, p. 114999, 2023.

[27] Q. Wu, Y. Qiao, R. Guo, S. Naveed, T. Hirtz, X. Li, Y. Fu, Y. Wei, G. Deng, Y. Yang, X. Wu, and T. L. Ren, "Triode-mimicking graphene pressure sensor with positive resistance variation for physiology and motion monitoring," *ACS Nano*, vol. 14, no. 8, pp. 10 104–10 114, Aug 2020.

[28] Y. Ni, L. Liu, J. Huang, S. Li, Z. Chen, W. Zhang, and Y. Lai, "Rational designed microstructure pressure sensors with highly sensitive and wide detection range performance," *Journal of Materials Science & Technology*, vol. 130, pp. 184–192, Dec 2022.

[29] S. Chen, Y. Song, and F. Xu, "Flexible and highly sensitive resistive pressure sensor based on carbonized crepe paper with corrugated structure," *ACS Applied Materials & Interfaces*, vol. 10, no. 40, pp. 34 646–34 654, Oct 2018.

[30] K. Singh, U. Valiyaneerilakkal, J. Akhtar, and S. Varghese, "Fabrication of poly (vinylidene fluoride-trifluoroethylene) – zinc oxide based piezoelectric pressure sensor," *Sensors and Actuators A: Physical*, vol. 303, p. 111677, Mar 2020.

[31] L. Huang, J. Chen, Y. Xu, D. Hu, X. Cui, D. Shi, and Y. Zhu, "Three-dimensional light-weight piezoresistive sensors based on conductive polyurethane sponges coated with hybrid cnt/cb nanoparticles," *Applied Surface Science*, vol. 548, p. 149268, May 2021.

[32] D. Kannichankandy, P. M. Pataniya, S. Narayan, V. Patel, C. K. Sumesh, K. D. Patel, G. K. Solanki, and V. M. Pathak, "Flexible piezoresistive pressure sensor based on conducting pani on paper substrate," *Synthetic Metals*, vol. 273, p. 116697, Mar 2021.

[33] S. Pyo, J. Lee, W. Kim, E. Jo, and J. Kim, "Multi-layered, hierarchical fabric-based tactile sensors with high sensitivity and linearity in ultra-wide pressure range," *Advanced Functional Materials*, vol. 29, no. 35, p. 1902484, Aug 2019.

[34] R. Qin, M. Hu, X. Li, T. Liang, H. Tan, J. Liu, and G. Shan, "A new strategy for the fabrication of a flexible and highly sensitive capacitive pressure sensor," *Microsystems & Nanoengineering*, vol. 7, no. 1, p. 100, Nov 2021.

[35] H. Guo, Y. J. Tan, G. Chen, Z. Wang, G. J. Susanto, H. H. See, Z. Yang, Z. W. Lim, L. Yang, and B. C. K. Tee, "Artificially innervated self-healing foams as synthetic piezo-impedance sensor skins," *Nature Communications*, vol. 11, no. 1, p. 5747, Nov 2020.

[36] R. B. Mishra, N. El-Atab, A. M. Hussain, and M. M. Hussain, "Recent progress on flexible capacitive pressure sensors: from design and materials to applications," *Advanced Materials Technologies*, vol. 6, no. 4, p. 2001023, Apr 2021.

[37] J. Hwang, Y. Kim, H. Yang, and J. H. Oh, "Fabrication of hierarchically porous structured pdms composites and their application as a flexible capacitive pressure sensor," *Composites Part B: Engineering*, vol. 211, p. 108607, Apr 2021.

[38] Y. Su, W. Li, X. Cheng, Y. Zhou, S. Yang, X. Zhang, C. Chen, T. Yang, H. Pan, G. Xie, and G. Chen, "High-performance piezoelectric composites via phase programming," *Nature Communications*, vol. 13, no. 1, p. 4867, 2022.

[39] D. Y. Park, D. J. Joe, D. H. Kim, H. Park, J. H. Han, C. K. Jeong, H. Park, J. G. Park, B. Joung, and K. J. Lee, "Self-powered real-time arterial pulse monitoring using ultrathin epidermal piezoelectric sensors," *Advanced Materials*, vol. 29, no. 37, Oct 2017.

[40] J. Yu, S. Xian, Z. Zhang, X. Hou, J. He, J. Mu, W. Geng, X. Qiao, L. Zhang, and X. Chou, "Synergistic piezoelectricity enhanced batio3/polyacrylonitrile elastomer-based highly sensitive pressure sensor for intelligent sensing and posture recognition applications," *Nano Research*, vol. 16, no. 4, pp. 5490–5502, Apr 2023.

[41] K. D. Novoselov, A. K. Geim, S. V. Morozov, D. Jiang, Y. Zhang, S. V. Dubonos, I. V. Grigorieva, and A. A. Firsov, "Electric field effect in atomically thin carbon films," *Science*, vol. 306, no. 5696, pp. 666–669, 2004.

[42] A. Ciesielski and P. Samorì, "Graphene via sonication assisted liquid-phase exfoliation," *Chemical Society Reviews*, vol. 43, no. 1, 2014.

[43] A. D. Smith, F. Niklaus, A. Paussa, S. Vaziri, A. C. Fischer, M. Sterner, F. Forsberg, A. Delin, D. Esseni, P. Palestri, M. Östling, and M. C. Lemme, "Electromechanical piezoresistive sensing in suspended graphene membranes," *Nano Letters*, vol. 13, no. 7, pp. 3237–3242, 2013.

[44] C. N. R. Rao, A. K. Sood, K. S. Subrahmanyam, and A. Govindaraj, "Graphene: the new two-dimensional nanomaterial," *Angewandte Chemie International Edition*, vol. 48, no. 42, pp. 7752–7777, Oct 2009.

[45] A. D. Smith, S. Vaziri, F. Niklaus, A. C. Fischer, M. Sterner, A. Delin, M. Östling, and M. C. Lemme, "Pressure sensors based on suspended graphene membranes," *Solid-State Electronics*, vol. 88, pp. 89–94, Oct 2013.

[46] V. Sorkin and Y. W. Zhang, "Graphene-based pressure nano-sensors," *Journal of Molecular Modeling*, vol. 17, no. 11, pp. 2825–2830, Nov 2011.

[47] K. I. Bolotin, K. J. Sikes, Z. Jiang, M. Klima, G. Fudenberg, J. Hone, P. Kim, and H. L. Stormer, "Ultrahigh electron mobility in suspended graphene," *Solid State Communications*, vol. 146, no. 9, pp. 351–355, Jun 2008.

[48] V. E. Dorgan, M. H. Bae, and E. Pop, "Mobility and saturation velocity in graphene on sio2," *Applied Physics Letters*, vol. 97, no. 8, Aug 2010.

[49] J. U. Lee, D. Yoon, and H. Cheong, "Estimation of young's modulus of graphene by raman spectroscopy," *Nano Letters*, vol. 12, no. 9, pp. 4444–4448, Sep 2012.

[50] S. C. Gong and C. Lee, "Analytical solutions of sensitivity for pressure microsensors," *IEEE Sensors Journal*, vol. 1, no. 4, pp. 340–344, Dec 2001.

[51] Y. Zhu, S. Murali, W. Cai, X. Li, J. W. Suk, J. R. Potts, and R. S. Ruoff, "Graphene and graphene oxide: synthesis, properties, and applications," *Advanced Materials*, vol. 22, no. 35, pp. 3906–3924, Sep 2010.

[52] A. T. Smith, A. M. LaChance, S. Zeng, B. Liu, and L. Sun, "Synthesis, properties, and applications of graphene oxide/reduced graphene oxide and their nanocomposites," *Nano Materials Science*, vol. 1, no. 1, pp. 31–47, Mar 2019.

[53] H. B. Yao, J. Ge, C. F. Wang, X. Wang, W. Hu, Z. J. Zheng, Y. Ni, and S. H. Yu, "A flexible and highly pressure-sensitive graphene–polyurethane sponge based on fractured microstructure design," *Advanced Materials*, vol. 25, no. 46, pp. 6692–6698, Dec 2013.

[54] A. Tewari, S. Gandla, S. Bohm, C. R. McNeill, and D. Gupta, "Highly exfoliated mwnt–rgo ink-wrapped polyurethane foam for piezoresistive pressure sensor applications," *ACS Applied Materials & Interfaces*, vol. 10, no. 6, pp. 5185–5195, Feb 2018.

[55] Y. A. Samad, Y. Li, A. Schiffer, S. M. Alhassan, and K. Liao, "Graphene foam developed with a novel two-step technique for low and high strains and pressure-sensing applications," *Small*, vol. 11, no. 20, pp. 2380–2385, May 2015.

[56] H. Tian, Y. Shu, X. Wang, M. Mohammad, Z. Bie, Q. Xie, C. Li, W. Mi, Y. Yang, and T. Ren, "A graphene-based resistive pressure sensor with record-high sensitivity in a wide pressure range," *Sci. Rep.*, vol. 5, no. 1, p. 8603, Feb 2015.

[57] C. B. Huang, S. Witomska, A. Aliprandi, M. A. Stoeckel, M. Bonini, A. Ciesielski, and P. Samori, "Molecule–graphene hybrid materials with tunable mechanoresponse: highly sensitive pressure sensors for health monitoring," *Advanced materials*, vol. 31, no. 1, p. 1804600, 2019.

[58] Z. Wu, J. He, H. Yang, and S. Yang, "Progress in aromatic polyimide films for electronic applications: Preparation, structure and properties," *Polymers*, vol. 14, no. 6, p. 1269, 2022.

[59] S. Vitale, H. Puozzo, S. Saiev, L. Bonnaud, A. Ricciardulli, A. Ciesielski, D. Beljonne, and P. Samorì, "Tuning the piezoresistive behavior of graphene-polybenzoxazine nanocomposites: Toward high-performance materials for pressure sensing applications," *Chemistry Of Materials*, vol. 35, pp. 6909–6919, 2023.

[60] A. Barlian, W. Park, J. M. Jr, A. Rastegar, and B. Pruitt, "Review: semiconductor piezoresistance for microsystems," *Proc. IEEE*, vol. 97, no. 3, pp. 513–552, 2009.

[61] Z. Yao, T. Liang, P. Jia, Y. Hong, L. Qi, C. Lei, B. Zhang, and J. Xiong, "A high-temperature piezoresistive pressure sensor with an integrated signal-conditioning circuit," *Sensors*, vol. 16, no. 6, p. 913, Jun 2016.

[62] Y. Liu, H. Wang, W. Zhao, H. Qin, and X. Fang, "Thermal-performance instability in piezoresistive sensors: inducement and improvement," *Sensors (Basel)*, vol. 16, no. 12, p. 1984, Dec 2016.

[63] A. D. Marcellis, C. Reig, and M. Cubells-Beltrán, "Current-based measurement technique for high sensitivity detection of resistive bridges with external balancing through control voltages," *IEEE Sens. J.*, vol. 17, no. 2, pp. 404–411, Jan 2017.

[64] A. Sanginario, I. Buraioli, M. Pogliano, P. Natale, D. Leone, G. Mingrone, A. Milan, and D. Demarchi, "Live demonstration: Wireless device for pulse wave velocity evaluation," in *2023 IEEE International Symposium On Circuits And Systems (ISCAS)*, 2023, pp. 1–1.

[65] A. Valerio, I. Buraioli, A. Sanginario, D. Leone, G. Mingrone, A. Milan, and D. Demarchi, "Live demonstration: Wireless device for clinical pulse wave velocity evaluations," in *2022 IEEE Biomedical Circuits And Systems Conference (BioCAS)*, 2022, pp. 247–247.

[66] D. Leone, I. Buraioli, G. Mingrone, D. Lena, A. Sanginario, F. Vallelonga, F. Tosello, E. Avenatti, M. Cesareo, A. Astarita *et al.*, "Accuracy of a new instrument for noninvasive evaluation of pulse wave velocity: the arterial stiffness faithful tool assessment project," *Journal Of Hypertension*, vol. 39, pp. 2164–2172, 2021.

[67] I. Buraioli, D. Lena, A. Sanginario, D. Leone, G. Mingrone, A. Milan, and D. Demarchi, "A new noninvasive system for clinical pulse wave velocity assessment: The athos device," *IEEE Transactions On Biomedical Circuits And Systems*, vol. 15, pp. 133–142, 2021.

[68] S. Conoci, F. Rundo, G. Fallica, D. Lena, I. Buraioli, and D. Demarchi, "Live demonstration of portable systems based on silicon sensors for the monitoring of physiological parameters of driver drowsiness and pulse wave velocity," in *2018 IEEE Biomedical Circuits And Systems Conference (BioCAS)*, 2018, pp. 1–3.

[69] I. Buraioli, D. Demarchi, A. Milan, F. Veglio, D. Leone, and F. Vallelonga, "Method and system for real-time measurement of the sphygmic wave velocity (pwv)," Patent, 2023, uS Patent App. 18/253,472.

[70] A. Valerio, I. Buraioli, A. Sanginario, G. Mingrone, D. Leone, A. Milan, and D. Demarchi, "A region-based cross-correlation approach for tonometric carotid–femoral pulse wave velocity assessment," *Biomedical Signal Processing And Control*, vol. 93, p. 106161, 2024.

[71] A. Valerio, I. Buraioli, A. Sanginario, D. Leone, G. Mingrone, A. Milan, and D. Demarchi, "A new true wireless system for real-time pulse wave velocity assessment," *IEEE Sensors Journal*, 2024.